UNIVERSITÀ DEGLI STUDI DI TRIESTE

Enhanced Photocurrent Generation in Proton-Irradiated “Giant” CdSe/CdS Core/Shell Quantum Dots

This is the peer reviewed (post-print) version of the following article:

Original
Enhanced Photocurrent Generation in Proton-Irradiated “Giant” CdSe/CdS Core/Shell Quantum Dots / Wang, C., Barba, D., Selopal, G.S., Zhao, H., Liu, J., Zhang, H., Sun, S., Rosei, F.. - In: ADVANCED FUNCTIONAL MATERIALS. - ISSN 1616-301X. - ELETTRONICO. - 29/2019:46(2019), pp. 1904501.1-1904501.11. [10.1002/adfm.201904501]

Availability:
This version is available at: 11368/3046167 since: 2023-05-19T22:23:49Z
Publisher:

Published
DOI:10.1002/adfm.201904501
Terms of use:

Some rights reserved. More details in the PostPrint rights section below.

License:
Digital Rights Management not defined

Publisher copyright

-.-

(Article begins on next page)

22 October 2026

arTs Università degli Studi di Trieste
Archivio della ricerca – postprint

Enhanced Photocurrent Generation in Proton-Irradiated "Giant" CdSe/CdS Core/Shell Quantum Dots

Chao Wang, David Barba, Gurpreet S. Selopal, Haiguang Zhao, Jiabin Liu, Hui Zhang, Shuhui Sun, and Federico Rosei**

Group II–VI quantum dots (QDs) possess tunable electrical and optical properties that make them very attractive for high-tech applications and power generation. The effects of proton irradiation on both the structural and physical properties of "giant" CdSe/CdS core–shell QDs (g-CS QDs) are investigated. These experiments shed light on photoelectron delocalization in g-CS QDs, where current linkages and strong variations in optical emission result from the spatial extension of the photoelectron wavefunctions over the conduction bands of CdSe and CdS. Monte Carlo simulations of ion–matter interactions show that the damaging rates can be set from the energy of impinging protons to promote the formation of structural defects in the core or shell. The formation of nanocavities is demonstrated after irradiation doses higher than ≈10^{17} H^+ cm^{-2}, while a continuous decrease in luminescence intensity is observed for increasing proton fluencies. This feature is accompanied by a concomitant lifetime decrease marking the rise of nonradiative phenomena and the occurrence of greater photocarrier transfers between CdS and CdSe. Current-to-voltage characterizations evidence that proton implantation can be implemented to enhance the photocurrent generation in g-CS QDs. This increase is attributed to the delocalization of photoelectrons in the CdS shell, whose improvement is found to promote electron–hole pair separation.

1. Introduction

Irradiation of solids with energetic particles, such as electrons or ions, gives rise to the formation of atomic defects that can strongly modify the material properties.[1] Both the understanding and the quantification of the effects induced by these radiations in nanostructured semiconductors provide physical insights and relevant information regarding their structural integrity, tunability, long-term degradation, and stability for numerous applications in materials science and optoelectronics, including space technology and power conversion. Beyond the natural protection provided by the Earth's atmosphere, various types of ionizing radiation (mainly composed of protons, alpha particles, gamma and X-rays) can be encountered.[2] This kind of environment is usually known to disrupt electronic systems and instrumentation, therefore it is important to evaluate the change in performance and test the stability of any system based on advanced materials. The effects of proton irradiations on solar cell performances,[3] field effect transistors,[4] and other optoelectronic devices[5] were studied extensively. It has been shown that the damage caused by incident particles induces irreversible changes in their physical properties, such as the shift of threshold voltage,[4] the modulation of electrical conductance,[4b] and the reduction of the photocarrier lifetime.[5b]

Colloidal quantum dots (QDs) are promising building blocks for several emerging technologies, due to their size/shape/composition-dependent optoelectronic properties based on quantum confinement.[6] QDs-based optoelectronic devices, such as photovoltaics (PV),[7] radiation sensors,[8] luminescent solar concentrators,[9,25] and light-emitting diodes,[10] can be potentially implemented in future technologies due to their extraordinary properties, high application potential, and low cost. For PV applications, the overlapping of excited electron wavefunctions inside and between the conduction and valence bands of nanostructured semiconductors makes possible the dissociation of excitons (e–h pairs) over a large spectral range.[11] The use of this wavefunction engineering can be applied to generate photocurrent[11c,12] and tune the optical properties of QDs.[11c,13]

Irradiation effects on both shape and morphology of nanoparticles (NPs) have been investigated for several types of NPs.[14] Here, we report such effects for core–shell systems, observed specifically in "giant" CdSe/CdS core–shell QDs (g-CS QDs). These materials were chosen because of their high stability over time.[7d] Previous works conducted on other nanomaterials

C. Wang, Dr. D. Barba, Dr. G. S. Selopal, J. Liu, H. Zhang, Prof. S. Sun, Prof. F. Rosei
Institut National de la Recherche Scientifique Centre Énergie Matériaux Télécommunications
1650 Boul. Lionel Boulet, Varennes, Québec J3X 1S2, Canada
E-mail: barba@emt.inrs.ca; rosei@emt.inrs.ca
Dr. G. S. Selopal, Prof. F. Rosei
Institute of Fundamental and Frontier Science
University of Electronic Science and Technology of China
Chengdu 610054, P. R. China
Prof. H. Zhao
State Key Laboratory of Bo-Fibers and Eco-Textiles and College of Physics
Qingdao University
No. 308 Ningxia Road, Qingdao 266071, P. R. China

showed that ion bombardment may affect the shape of the irradiated NPs.[14b] In addition to the morphological changes, some studies also demonstrated that ion irradiation can create defects or induce structural phase transitions.[15] Regarding the changes induced in materials properties, irradiation experiments on Si QDs embedded in SiO_2[16] indicate that increasing the ion dose decreases both the luminescence intensity and the lifetime of Si QDs at 800 nm. Similar Si/SiO_2 systems exposed to H^+, He^+, Si^+, Ge^+, and Au^+ ion beams exhibit a strong decrease of the QDs luminescence intensity. Nevertheless, for single-layer InGaAs/GaAs QDs,[7d,17] multilayer InAs QDs[18] and colloidal CdSe/ZnS QDs embedded in polymers[19] exposed to various proton beams, stronger luminescence was reported after irradiation. Although semiconducting QDs have been used as efficient absorber/emitters for different types of optoelectronic devices,[7b–d,8a,b] the investigation of the ion irradiation stability is still largely unknown, especially for colloidal "giant" core/shell QDs.

Here, we performed proton irradiation on g-CS QDs system. We used the stopping and range of ions in matter (SRIM) Monte Carlo simulation code to evaluate the damage resulting from the ion–matter interaction for 1.5 and 10 keV energies and ion fluences up to 10^{17} H^+ cm^{-2}, which corresponds to radiation exposure conditions for long-term operation on Earth and durations longer than several decades in outer space.[2b] The results indicate that ion implantation can be used to generate different damaging rates into core–shell structures and tune their physical properties by setting the acceleration energy.

Structural investigations at the atomic scale were conducted by high-resolution TEM (HRTEM), followed by photoluminescence (PL), transient PL measurements, and current-to-voltage (*I*–*V*) characterizations to study their evolution upon the irradiation doses. Nanocavities with a diameter of ≈1.0 nm are reported for g-CS QDs exposed to strong proton fluences. The density of nanocavities observed by TEM is found to be consistent with the rate of vacancies generated during irradiation, according to SRIM simulations.[20] Both the PL intensity and lifetime of QDs decrease after irradiation. By comparing the measurements obtained for experiments conducted with ion beams of 1.5 and 10 keV, the reduction of these two parameters appears to vary linearly with the concentration of surface defects/traps created by impinging protons into the CdS shell. The *I*–*V* curves of QDs deposited on Si and irradiated with 1.5 and 10 keV H^+ show that the semiconductor bandgaps and the charge carrier exchanges inside and outside QDs differ from the *I*–*V* response of the substrate. These variations are attributed to the generation of additional nonradiative decay channels in the g-CS QDs system, as well as efficient photoelectron delocalization. Under illumination, we evidence the occurrence of enhanced photoelectron exchanges and electron/hole separation in systems containing more defects inside their CdS shell, which both promote the photocurrent generation.

2. Results and Discussion

2.1. Proton Implantations into g-CS QDs

The SRIM Monte Carlo code was used to simulate the ion beam implantation conditions and the resulting processing of materials. The code is based on the binary collision approximation approach.[20] For the convenience of the SRIM simulations, we built a simple three-layer model with a 3 nm layer thickness (**Figure 1**). The thickness of each layer is defined by the shell thickness and the core diameter of the g-CS QDs. The rate of damage generated by impinging protons depends on their energy, tilt angle, as well as the density and atomic composition of the target. Two different acceleration voltages of 1.5 and 10 keV were set, to promote the formation of vacancies either in the shell or in the core, respectively. For such energies, it is found that more than 89% of the impinging protons cross the g-CS QDs entirely. SRIM 2013 full-cascade simulations performed with CdSe density of 5.82 g cm^{-3} and CdS density of 4.82 g cm^{-3} are presented in Figure 1. The maximum penetration depth of the impinging protons calculated using these simulations in the target is ≈80 and ≈260 nm, for acceleration voltages of 1.5 and 10 kV, respectively. Figure 1a,b shows the depth-distribution of the vacancies created by 1.5 and 10 keV proton irradiations, respectively. Nuclear collisions are usually higher for low proton energies (Figure S1, Supporting Information), so that an implantation conducted for acceleration voltage of 1.5 kV generates more vacancies. The latter is related to recoiled target atoms that were displaced from their original site. The plot ordinate units are given in vacancy per ion so that the total vacancy concentration can be directly obtained from the ion-beam current and the irradiation times that are measured during each experiment. The results presented in Figure 1a,b indicate that 1.5 and 10 keV proton irradiations create almost the same rate of vacancies inside the CdSe core, while 1.5 keV proton irradiation creates 30% higher vacancies in the CdS shell than that of 10 keV protons. Such features remain qualitatively valid for two stacked g-CS QDs exposed to 1.5 and 10 kV proton beams, as shown by the SRIM damage profiles presented in Figure S2 (Supporting Information), where the solid lines in green refer to the relative fraction of vacancies generated in the CdS shell, and the solid lines in red refer to the ones generated in the CdSe core. This indicates that the ion implantation energies can be set to control the formation of structural defects in different regions of the samples, even for multilayered g-CS QDs.

2.2. Structural Effects of Proton Bombardment in Implanted QDs

Bright field (BF) (**Figure 2**a) and HRTEM (Figure 2b) images show g-CS QDs with narrow size distribution and clear crystalline lattice. The inset selected area electron diffraction (SAED) pattern in Figure 2a demonstrates that the g-CS QDs have wurtzite (WZ) crystal structure (JCPDS No. 00-041-1049). Before proton beam exposure, the individual QDs exhibit uniform TEM contrast except few QDs that contain stacking faults.[21] The crystal plane *d*-spacing in Figure 2b is measured to be ≈3.16 and ≈3.58 Å with an angle of ≈63.9°, which corresponds to the $(10\bar{1}1)$ and $(10\bar{1}0)$ plane of WZ crystal structure of CdS.[22] After proton irradiation of 1×10^{17} H^+ cm^{-2}, the TEM contrast of individual QDs (Figure 2c,e) is not as uniform as the one reported before irradiation (Figure 2a,b). Both BF and HRTEM images reveal the appearance of small white spots, pointed out by arrows in Figure 2c,e. This feature is

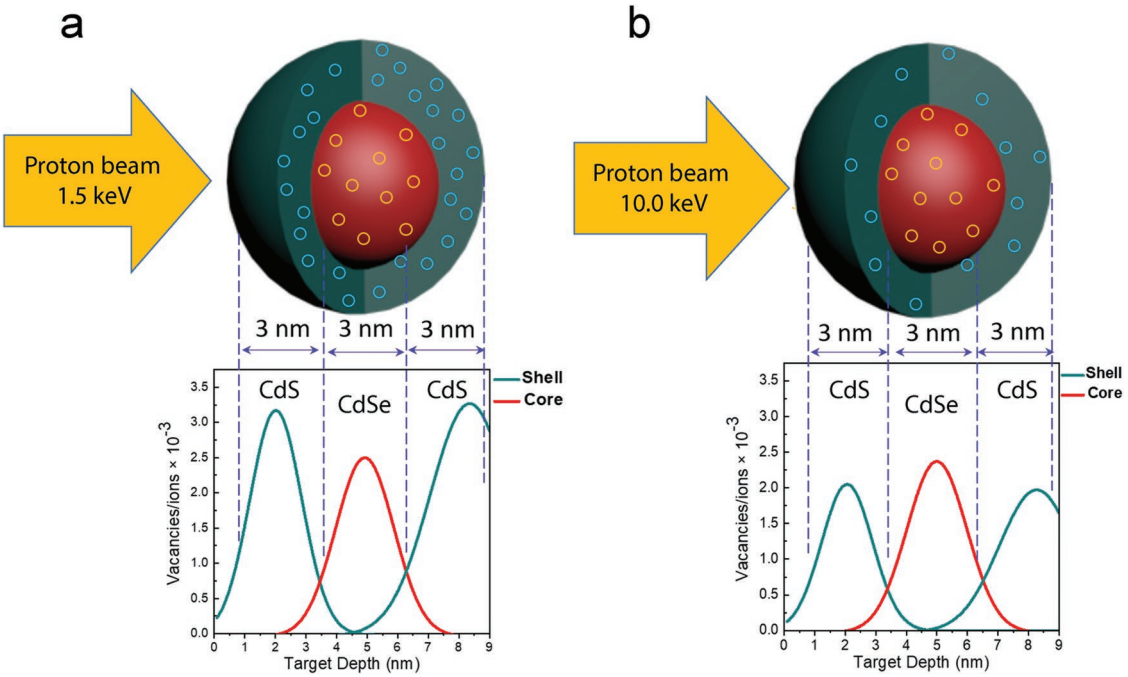

Figure 1. a,b) Vacancy distribution calculated from SRIM simulations, inside g-CS QDs exposed to 1.5 and 10 keV proton beams.

corroborated by the modulation of the HRTEM contrast intensities along with the directions drawn on each image, indicating significant changes after irradiation.

Nevertheless, Figure 2d,f shows that the crystalline lattice is still ordered, showing $\{10\bar{1}0\}$ and $\{10\bar{1}1\}$ lattice planes that were used to determine both *d*-spacings and interplanar angles. After proton irradiation, no volume expansion is observed, since the crystal plane *d*-spacings are still consistent with the ones of bulk WZ CdS (JCPDS No. 00-041-1049). This confirms that the impinging protons go through the whole QDs and that less than 10% are stopped inside the irradiated g-CS QDs during experiments.[20] The inset SAED patterns in Figure 2c,e also indicate the crystal structure of QDs survived to 1×10^{17} H^+ cm^{-2} irradiations. For defect-free QDs, the nonuniform TEM contrast mainly arises from mass-thickness contrast.[23] Therefore, the white spots formed in the QDs can be associated with nanoscale cavities.

To clarify the formation of nanocavities, proton irradiations were conducted for ion doses varying between 1×10^{14} and 1×10^{17} H^+ cm^{-2}, followed by TEM observations. The low-magnification (120 000×) TEM images are shown in Figure S3 (Supporting Information) and those recorded at higher magnification (400 000×) are presented in **Figure 3**, for proton irradiations at fluences between 1×10^{16} and 1×10^{17} H^+ cm^{-2}. Although all irradiated QDs are damaged, the TEM image contrast is observed to depend on the experimental parameters (electron beam aperture, intensity, and magnification), sample thickness, and the crystal orientation of each g-CS QD, indicating that the sharpness of the nanocavities is nonuniform. The images presented in Figure 3a–c show that the nanocavities start to form for 10 keV proton energies with implanted ion doses higher than 5×10^{16} H^+ cm^{-2}. In addition, the size of the formed nanocavities is found to increase with the proton fluence. For ion doses lower than 5×10^{16} H^+ cm^{-2}, no significant change was observed.

The formation of nanocavities can be explained as follows: During proton irradiation, the impinging protons have successive collisions with the target atoms of QDs. After collision, if the energy transfer to the target atom is larger than the binding energy of a lattice atom to its site, a vacancy can form. In a particular area of QDs, only if the number of atoms knocked out by impinging protons is large enough, a cavity will be found. Objects smaller than 1 nm are not accounted for in our study because there are close to the detection limit of the TEM (around 0.6 nm). We can nevertheless assume that nanocavities with diameters smaller than 1 nm can form during irradiation. According to SRIM calculations, which show the distribution of damage inside bombarded QDs in Figure 1c, the density of vacancies created by 10 keV proton irradiation at 1×10^{17} H^+ cm^{-2} is about 2 nm^{-2}. For an average QD area of 65 nm^2, this corresponds to about 130 vacancies per QD. Considering that one nanocavity consists of 10–20 vacancies, the average number of nanocavities inside each QD should be between 6 and 13. This rough estimation is consistent with the number of nanocavities observed by TEM (Figure 3c), where the surface concentration of nanocavities is found to be around 10 per QD. The estimation method can also be used in the case of lower proton fluence irradiation (Figure 1b).

2.3. Optical Effects of Impinging Protons on QDs

All samples were measured at room temperature with the same active area (≈2 mm^2), to compare the optical properties of QDs before and after irradiation. **Figure 4**a,b shows the absorption and PL spectra of g-CS QDs before and after irradiation with

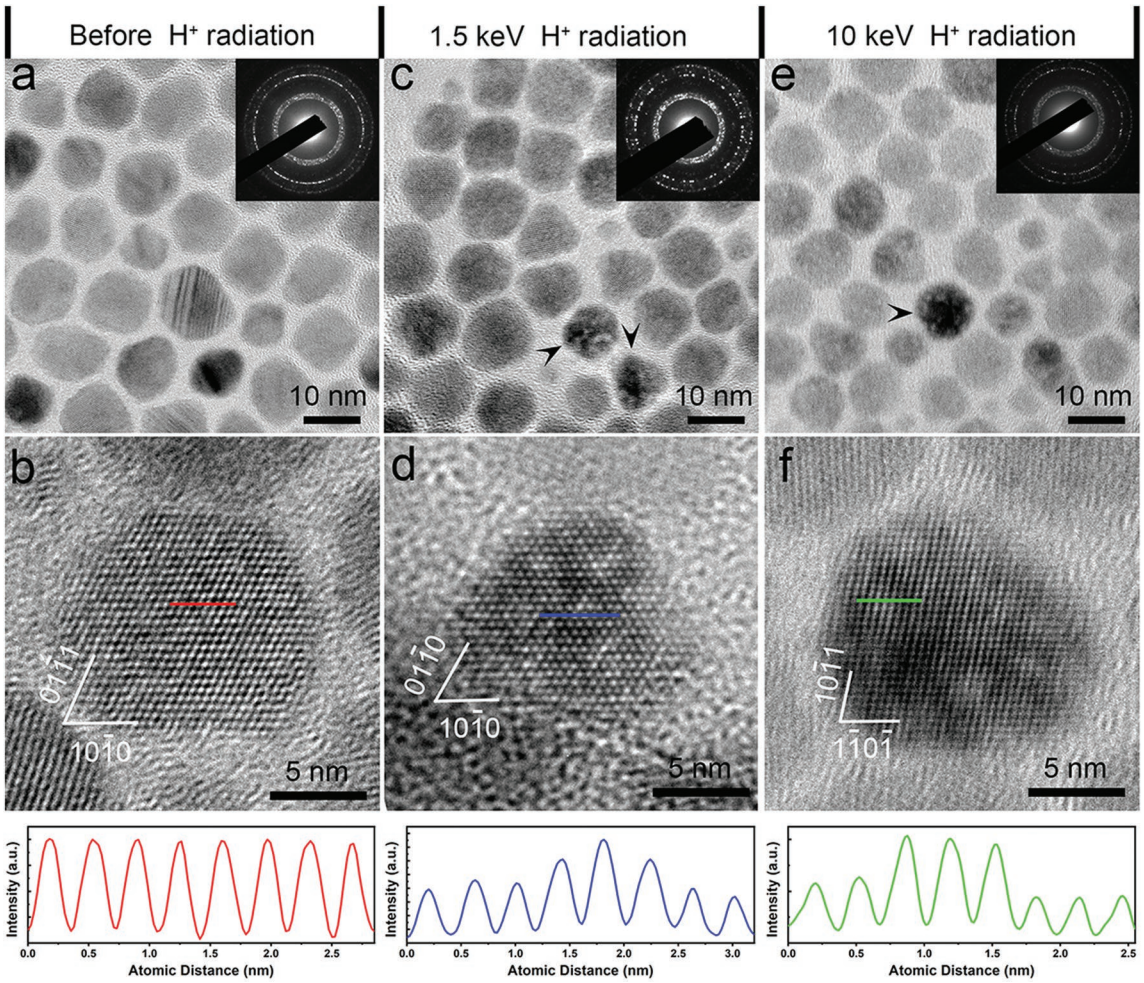

Figure 2. BF images, HRTEM images, and intensity profiles of g-CS QDs: a,b) before irradiation; c,d) after 1.5 keV proton irradiation at 1×10^{17} H^+ cm^{-2}; e,f) after 10 keV proton irradiation at 1×10^{17} H^+ cm^{-2}.

1.5 and 10 keV proton energies at ion doses varying between 5×10^{13} and 5×10^{15} H^+ cm^{-2}. Before irradiation, all samples show a strong PL emission with a PL peak around 627 nm. In Figure 4a,b, while the PL intensity of QDs after proton irradiation is found to decrease with the irradiation dose, neither shift nor spectral changes are measured. A similar variation in PL emission was recorded in preliminary studies conducted on core CdSe QDs exposed to 20 keV protons, as presented in Figure S4 (Supporting Information). The behavior reported in this work for g-CS QDs exposed to 1.5 and 10 kV proton beams differs from the results obtained by Zanazzi et al. for CdSe/ZnS QDs embedded in polyvinyl alcohol (PVOH),[19] who observed a decrease followed by an increase of the QD PL emission after 2 MeV proton irradiations, due to the activation of charge carrier transfers between the QDs and the irradiated matrix of PVOH. As the materials we have investigated by photoluminescence measurements are freestanding g-CS QDs dispersed on a silicon wafer, no contribution from their surrounding is expected before and after irradiation, so that their PL emission decreases continuously with the proton irradiation dose.

Our observation also highlights that both the size and bandgap of g-CS QDs remain unchanged after irradiation.[22] This feature is qualitatively consistent with the slight decrease reported in optical absorbance after exposure to the proton beam. In Figure 4c,d, the normalized spectral intensity of each measured PL peak is reported as a function of the proton fluence and the corresponding concentration of irradiated-induced vacancies that were determined within the CdS shell using the SRIM calculations presented in Figure 1. The intensity of the PL signal was obtained after subtracting the optical background contribution and numerical integration of the PL peak between 550 and 750 nm. As shown in Figure 4c, 1.5 keV proton irradiation exhibits a slightly faster reduction of PL intensity than for the case of 10 keV. In Figure 4d, the linear decrease of this signal upon the concentration of vacancies generated by impinging protons inside the CdS shell indicates that the faster decrease reported for low-energy irradiations results from the higher damaging rate and the greater nuclear collision cross section between 1.5 keV protons and target atoms. Such a remark is consistent with the vacancy distribution calculated from SRIM simulations in Figure 1a, as well as the nuclear stopping power presented as a function of the proton energy in Figure S1 (Supporting Information).

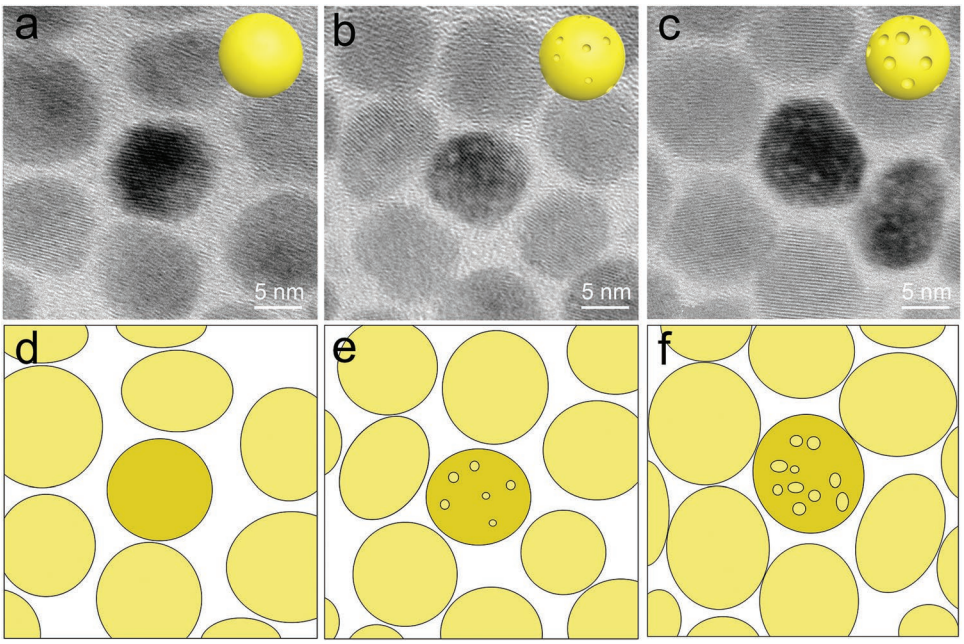

Figure 3. TEM images and sketches of g-CS QDs after 10 keV proton irradiation with fluence of a,d) 1×10^{16} H^+ cm^{-2}, b,e) 5×10^{16} H^+ cm^{-2}, and c,f) 1×10^{17} H^+ cm^{-2}, respectively.

The fluorescence decays of QDs under optical excitation at λ_{ex} = 444 nm are shown in **Figure 5**a,b. After proton irradiation, all PL lifetimes are found to decrease with the dose of implanted protons. The representative fluorescence decay curves of the PL peak centered at 627 nm of g-CS QDs were fitted using triple exponential decay functions. The intensity-weighted average lifetime $\langle\tau\rangle$ is estimated using the following equation[22,24]

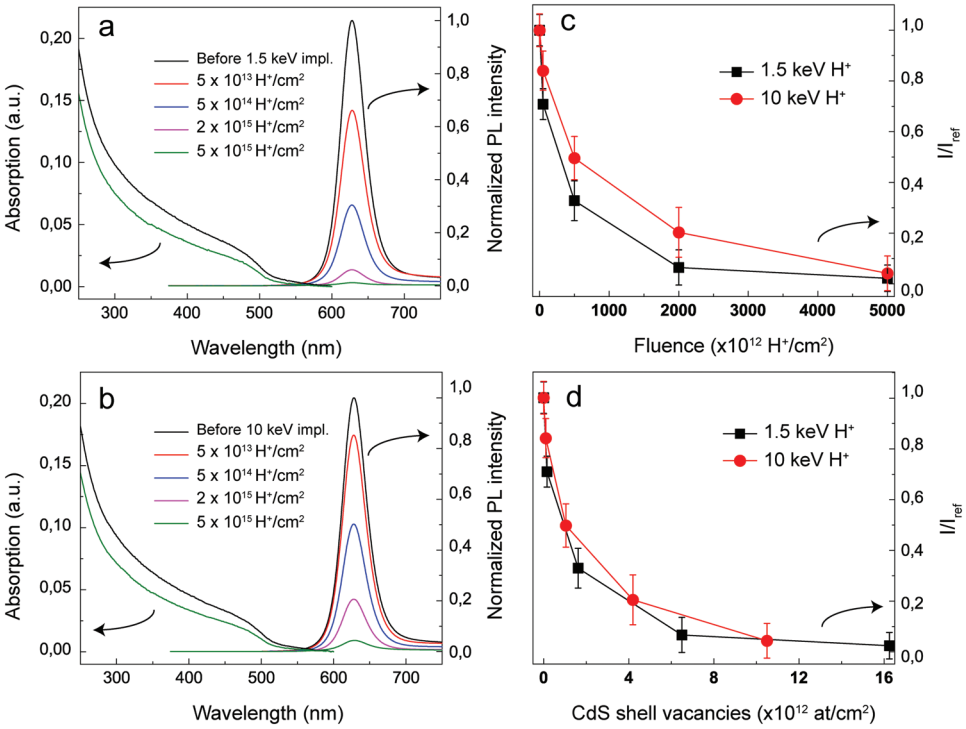

Figure 4. a,b) Evolution of the absorption and PL spectral emission in g-CS QDs exposed to1.5 and 10 keV proton irradiation, c) with the dose-dependence of the PL signal integrated between 550 and 700 nm, and d) as plotted as a function of the variation in CdS shell vacancy surface concentration calculated by SRIM.

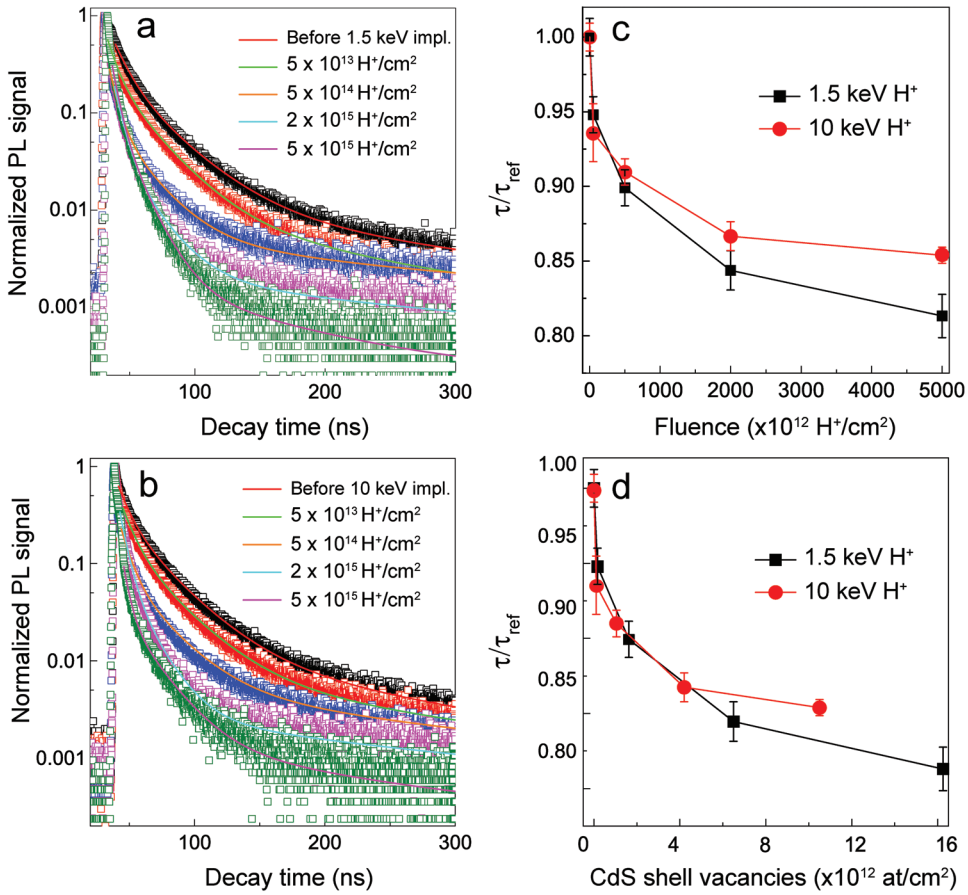

Figure 5. Evolution of the PL decay. a,b) g-CS QDs under 1.5 and 10 keV proton irradiation; c) dose-dependence of PL lifetime and d) its variation upon the surface density of CdS shell vacancies calculated by SRIM.

$$\tau = \frac{\sum a_i \tau_i^2}{\sum a_i \tau_i} \tag{1}$$

where a_i are the coefficients of the fitting of PL triple exponential decay (i = 1, 2, 3). Before irradiation, the measured lifetime of as-prepared g-CS QDs is 66.6 ns. After 5×10^{15} H^+ cm^{-2} irradiation, the measured lifetimes decrease to 54.1 and 57.0 ns for 1.5 and 10 kV acceleration voltages, respectively.

As observed in Figure 4d for the variation of the PL intensity upon irradiation, a faster decrease of the average lifetime of photocarriers is observed after exposure to proton beams of lower energy in Figure 5d. Such a behavior is also qualitatively consistent with the higher formation rate of vacancies inside the g-CS QDs target for 1.5 keV impinging protons (Figure 1b,c). This confirms the role played by CdS shell on the g-CS QD luminescent properties, related to electron delocalization effects.[7d,17]

The variations of radiative decay rate (K_{et}) and nonradiative decay rate (K_{net}) after proton irradiations can be extracted from the fluorescence quantum yield (QY), which is related to the variations of lifetime measured by time-resolved PL spectroscopy,[25] as follows

$$\mathrm{QY} = \frac{K_{et}}{K_{et} + K_{net}} \tag{2}$$

where the measured lifetime is defined as

$$\tau = \frac{1}{K_{et} + K_{net}} \tag{3}$$

Before proton irradiation, the average QY of as-synthesized g-CS QDs is found to be ≈45%, as reported in the literature.[22]

Based on the relative QY calculated through the variation of PL intensity (Figure 4) and absorption (see Figure S5, Supporting Information), the values of K_{et} and K_{net} can be calculated from Equations (2) and (3). As shown in **Figure 6**, the values of K_{et} decrease with the fluence, while values of K_{net} increase. The higher nonradiative decay rate K_{net} arises from the formation of surface defects/traps induced by the irradiation process.[16,25,26] These surface defects/traps will open up new nonradiative decay channels and highly affect the lifetime of photocarriers inside the core–shell heterostructure system. The occurrence of such effects is consistent with TEM imaging (Figure 2) and is also supported by SRIM simulations (Figure 1). This suggests that the nanocavities formed during irradiations can act as new nonradiative centers.

In Figure 6, the increase of K_{net} is also found to be 10% higher for 1.5 keV irradiations than for the ones at 10 keV. Such a variation is substantially lower than the increase by 30% of the vacancies generated in samples exposed to a proton beam of

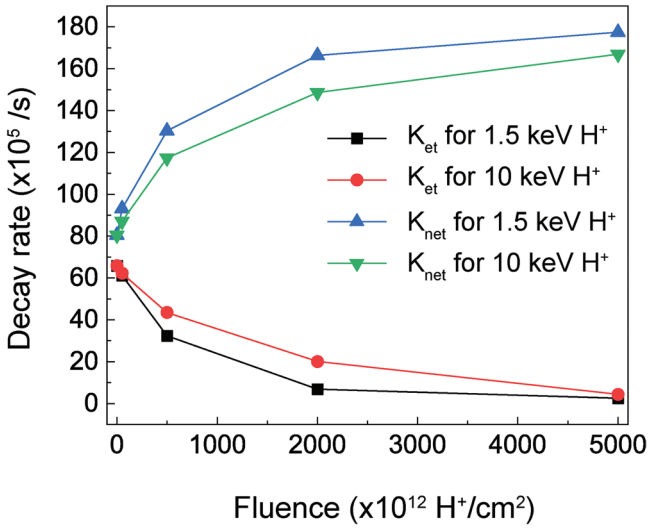

Figure 6. Evolution of K_{et} and K_{net} of g-CS QDs under proton irradiation.

lower energy. This leads to two observations: First, the number of nonradiative centers differs from the number of vacancies located within the medium;[27] Second, the overdamaging of the CdS shell shown for 1.5 keV proton irradiations (Figure 1b) should reduce the contribution of delocalized photocarriers to the PL emission process due to the generation of more nonradiative traps. This latter effect would be consistent with the results presented in ref. [22] indicating that a fraction of about 40–50% of the optically excited photocarriers is delocalized over the whole core–shell systems and contribute to the increase in both global PL emission and average PL lifetime.

2.4. *I–V* Characterizations and Photocurrent Generation

The g-CS QDs were dispersed on p-type Si substrates bonded to a copper plate using silver paste. To measure the effect of proton implantations on both the electrical properties and the photocurrent generation, the studied samples were covered by a 20 nm MoO_3 film, followed by a top Au electrode of 17 nm thickness. Both MoO_3 and Au layers were deposited by evaporation after ion exposure. To verify that the H^+ ions implanted into the QDs/Si targets did not contaminate or affect the chemical structure of the MoO_3 films,[28] their chemical composition has been investigated by XPS measurements in nonimplanted and implanted samples. As shown in Figure S6 (Supporting Information), no significant change is observed in the $3d_{5/2}$ and $3d_{3/2}$ valence bands of Mo. Both are found to be dominated by Mo^{6+} states.

The *I–V* curves of MoO_3/QDs/Si and MoO_3/Si systems under dark and 1 sun solar-simulated illumination (AM 1.5G, 100 mW cm^{-2}) are presented in **Figure 7**, for applied bias voltages varying between −1.5 and +1.5 V. Figure 7a,b corresponds to samples containing QDs, before and after implantations performed at 1.5 and 10.0 kV, respectively. For each implantation energy, the doses of implanted protons were set to generate the same amount of vacancies inside the whole g-CS structure (Figure 1). Figure 7c,d are related to data recorded for pure silicon wafers exposed to similar proton beams.

In the following discussion, the "forward" (and "reverse") bias polarizations are defined as the positive (and the negative) terminals of the voltage generator connected with the upper electrode. Accordingly, the right part of each figure related to applied voltages between 0.0 and +1.5 V corresponds to forward bias *I–V* measurements, and the left one (between −1.5 and 0.0 V), to the reverse ones, respectively. For all experiments conducted in dark conditions, the forward current passing through the MoO_3/QDs/Si or the MoO_3/Si systems is measured to be greater than the reverse current. A decrease in the reported values is also observed with the increase of the proton beam exposure. These two features appear to occur faster and/or to be more pronounced for implantations conducted at 1.5 kV and those conducted at 10.0 kV. For *I–V* curves obtained under illumination, the measurements strongly differ in the presence and absence of g-CS QDs. Two remarkable and very distinct trends are reported. First, almost no reverse biased photocurrent is detected in MoO_3/QDs/Si samples (left parts of Figure 7a,b), whereas a strong current is observed in the MoO_3/Si systems (left parts of Figure 7c,d). Second, while all measured photocurrents are found to decrease with the proton dose in implanted MoO_3/Si (Figure 7c,d), these photocurrents are found to increase continuously with the H^+ fluencies in MoO_3/QDs/Si (Figure 7a,b). This latter effect is highlighted by the four vertical arrows (in yellow) that have been directly reported in Figure 7.

The degradation of the biased current after proton-beam exposures and the decrease of its related photocurrent are consistent with the increase of structural "modification" and optical delocalization, both presented in Sections 2.3 and 2.4. In such a scenario, the observed losses may result from the increase of current leaks in the conduction and valence bands of irradiated QDs, as well as in the upper part of the Si substrate where implanted protons are located. Nevertheless, a more detailed clarification is needed to explain the difference in forward and reverse currents, as well as the significant improvement of the photocurrent generation reported for MoO_3/QDs/Si systems on Figure 7a,b.

In **Figure 8**a, we propose a complete description of the bandgap alignment occurring in MoO_3/QDs/Si systems, based on previous investigations conducted on g-CS QDs,[7d] as well as UV photoelectron spectroscopy (UPS) measurements carried out in silicon substrates before and after exposure to different H^+ beams (see Figure S7, Supporting Information). On the left of Figure 8a, the type-II heterojunction between MoO_3 and the CdS shell of the QDs is comparable to the bandgap interfaces of TiO_2/CdS[7d] and bulk MoO_3/CdS layers found in the literature,[29] for given bandgap energies of 3.1 and 2.7 eV, in MoO_3 and CdS, respectively. The bandgap of the CdSe core is 1.8 eV, in agreement with the expected PL spectra presented in Figure 4a,b.[7d,30] An indirect bandgap of 1.1 eV is chosen to illustrate the type I junction between the bottom side of the CdS shell and the top surface of the implanted Si layer.[31] As the generation of bi-vacancies in implanted Si is known to increase the concentration of donor states inside the medium,[29a] the increase of the valence band edge and the slight decrease of the sample work functions reported in Figure S7 (Supporting Information) indicate that the band structure of the Si substrate exposed to proton bombardment is upshifted by 0.2–0.3 eV

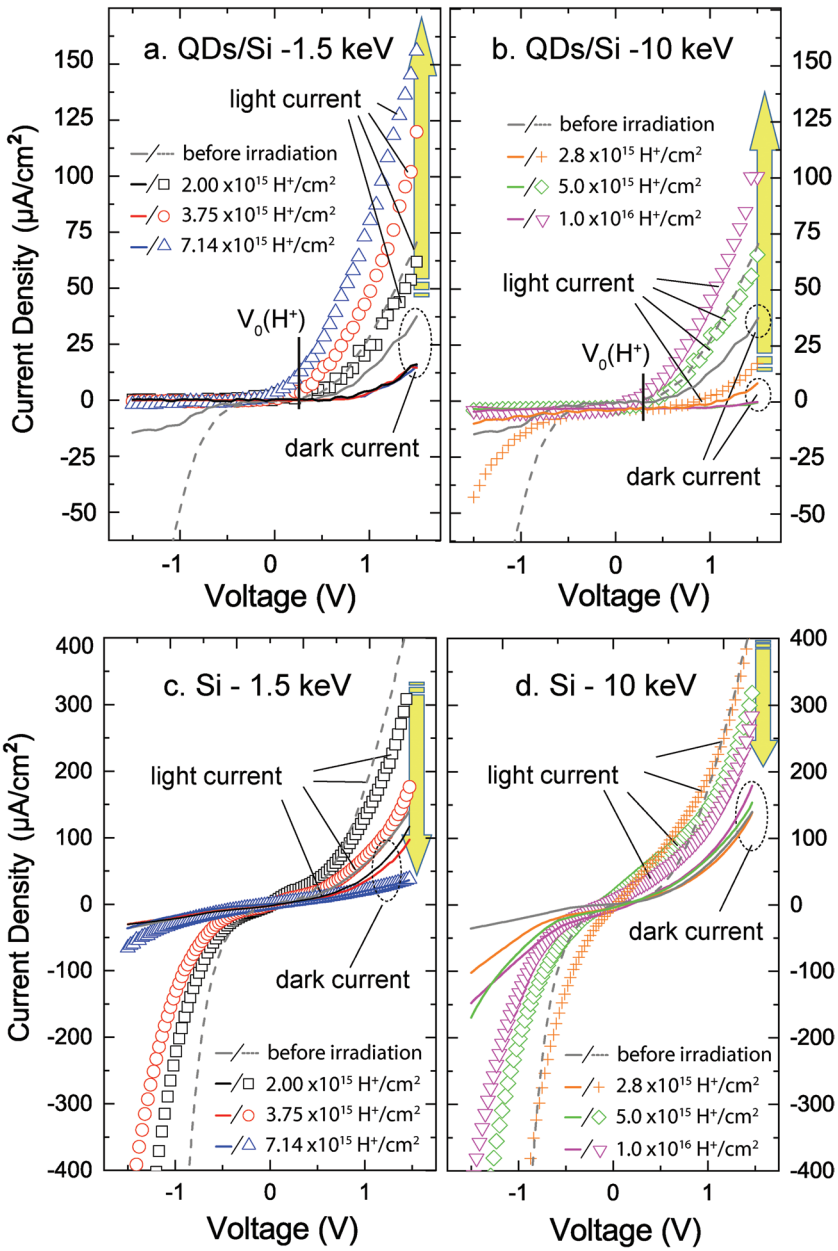

Figure 7. *I–V* characteristics of MoO_3/QDs/Si and MoO_3/Si under dark and illumination, a,b) for QDs implanted at 1.5 and 10.0 kV, as well as c,d) Si substrates implanted at 1.5 and 10.0 kV.

with respect to that of nonimplanted Si. The junction between the implanted Si layer (labeled "Si_{H+}" on the figure) and nonimplanted Si region located deeper than several hundreds of nm is assimilated to a type II energy barrier, as illustrated in the right part of Figure 8a and zoomed in Figure 8b. According to SRIM calculations,[20] the thickness of the Si_{H+} layer is of about 80 and 260 nm for 1.5 and 10.0 keV ion beams, respectively. For the whole system, the bandgap alignment is set with respect to the Fermi level shown by the horizontal dashed line in Figure 8a–c.

The presence of the CdS/Si_{H+}/Si interface can explain the evolution of *I–V* curves in reverse and forward polarizations. The lower value of the conduction band minimum in the Si_{H+} sublayer and the higher value of its valence band maximum create energy barriers for electrons passing through the implanted Si layer toward the CdS shell or the Si substrate. These barriers generate two local electric fields of opposite directions (labeled E_1 and E_2 in Figure 8b) resulting from the equilibrium of the donor/acceptor distributions across the Si_{H+}/Si and Si_{H+}/CdS junctions. The Si_{H+}/CdS interface has an energy barrier of about 0.5–0.6 eV, which is twice the one of Si-H/Si (≈0.3 eV). In the first approximation, the total contribution of charge carrier redistribution can be averaged inside the Si_{H+} "buffer" layer as a positive electric field, *E*, oriented normal to the Si substrate (Figure 8b). In the right part of Figure 8c, a schematic representation of the CdS/Si_{H+}/Si heterojunctions is presented.

For reverse bias, the average energy barrier potential between the CdS core and the Si substrate: $\Phi = q(E - V)$ increases, so that the charge carrier transfers between QDs and Si decreases and the current passing through the MoO_3/QDs/Si system is reduced. These effects are evidenced in the left parts of Figure 7a,b, where reverse biased current densities are lower than 1. μA cm^{-2}. Conversely, the forward polarization favors the current flow through the device by reducing the energy barrier Φ. This feature leads to higher forward bias conductivity, as seen in Figure 7a,b. The applied voltage for which Φ = 0 eV (labeled $V_0(H^+)$ on Figure 7a,b) refers to acceleration tension thresholds varying between +0.1 and +0.2 V, above which forward biased current densities higher than 10 μA cm^{-2} are recorded. Although this quantity was not found to vary continuously with the irradiation dose, its value should depend on the concentration of structural defects induced by proton bombardment.

The strong discrepancy between forward and reverse polarizations is not observed in MoO_3/Si systems without g-CS QDs. For this set of samples (Figure 7c,d), the measurement of greater reverse biased currents reveals the formation of a type II junction between MoO_3 and Si_{H+}, as already stated for bulk MoO_3/Si heterojunctions.[31] After implantation, the presence of structural defects inside the Si substrate is found to have a limited impact on the *I–V* characteristics, because the conduction band minimum and the valence band maximum of the Si_{H+} sublayer remain always greater or equal to the ones of MoO_3 (Figure 8a).

Under 1 sun illumination, the photocurrent generation process occurring in MoO_3/QDs/Si systems is described in Figure 8c. As calculated by Selopal et al. in CdSe/CdS,[7d] the excitons created inside the CdSe/CdS QDs are made of electrons whose spatial wavelength function is delocalized over the CdSe-CdS core–shell conduction band, and holes that are

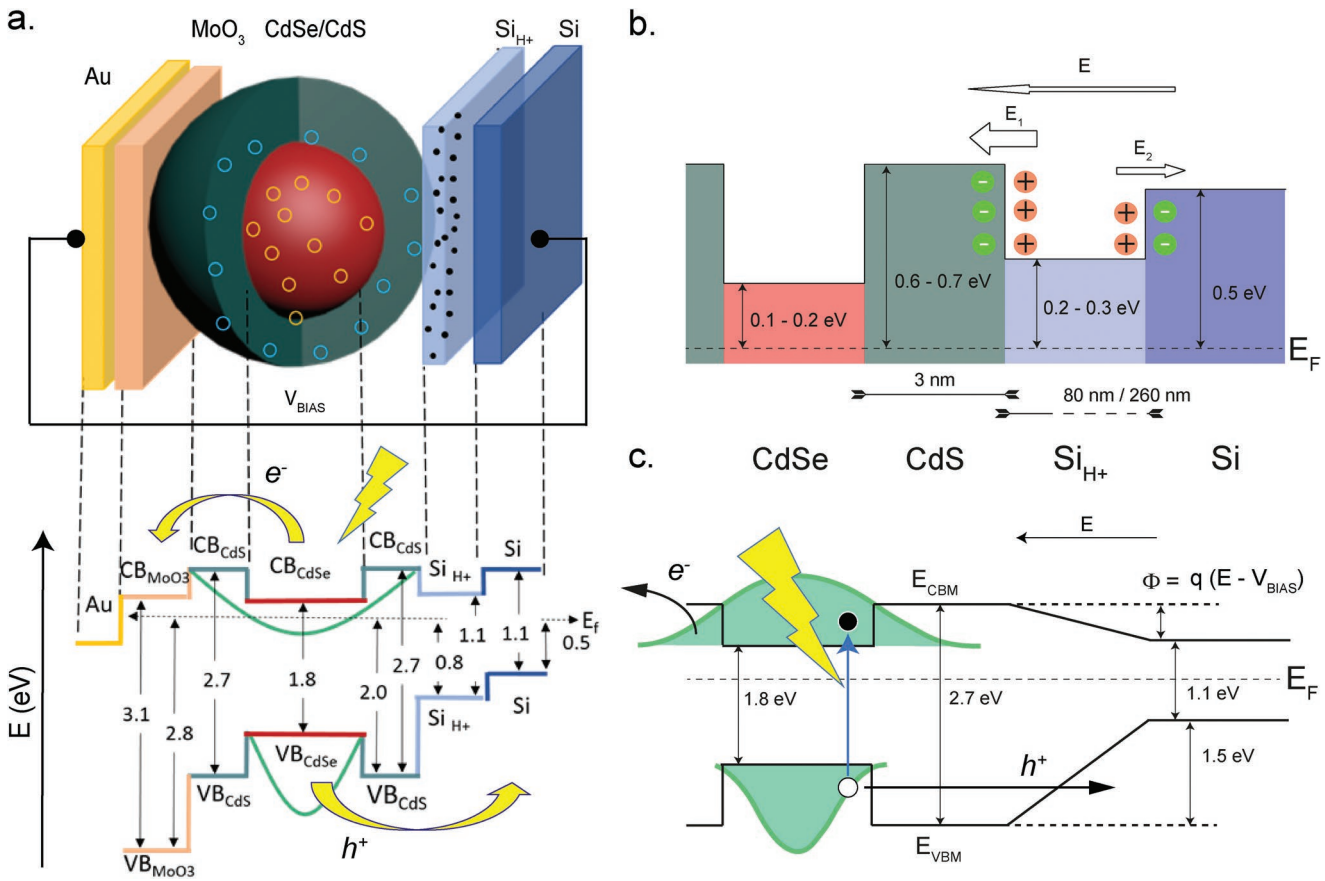

Figure 8. a) Schematic band alignment along the Fermi level in MoO_3/QD/Si systems containing g-CS QDs, b) donor/acceptor redistribution at CdS/Si-H and Si-H/Si interfaces leading to local electric fields E_1 and E_2. c) Equivalent potential downshift, Φ, given upon $E = E_1 - E_2$ and the biased voltage, V_{BIAS}, with the enhanced photovoltaic process due to the delocalization of conduction electrons in the g-CS system.

located within the valence band of the CdSe core. Such a configuration was found to reduce the spatial electron–hole (e–h) overlap and improve the exciton dissociation. It can be implemented to enhance the electron injection from the conduction band of the QDs into the conduction bands of their neighboring semiconductors.[32]

In proton-irradiated g-CS systems, where the PL emission and optical properties of QDs indicate the occurrence of stronger delocalization effects (Section 2.3), we infer that the presence of an increasing number of nonradiative structural defects favors electron exchanges between the superimposed and overlapped wavefunctions of the CdSe/CdS conduction bands. This enhanced electron delocalization over the core–shell system promotes the electron–hole pair separation induced by charge carrier transfers inside and at the QD interfaces. Such a feature would explain the generation of stronger forward light currents reported in Figure 7a,b, as well as the continuous increase of the current density upon the dose of implanted protons. From the variation in the forward current measured with an applied voltage of +1 V under solar illumination in irradiated systems, we found a significant increase in photocurrent density relative to the current density measured in nonimplanted MoO_3/QDs/Si. This enhancement is higher than 100% for QDs exposed to 1.5 keV protons that generate stronger structural and optical changes in the materials, and around 50% for 10 keV proton bombardments. Nevertheless, the QDs spread on the Si wafer before implantation and the deposition of MoO_3 do not form a homogenous layer of uniform thickness. The measurements conducted in MoO_3/QDs/Si samples and presented in Figure 7a,b also account for the contribution of MoO_3 that was directly deposited on the Si wafer or the Si_{H+} sublayer, due to the spacing existing between each QD. This makes thus impossible a precise quantification of both the photocurrent generation in QDs and its improvement caused by their proton irradiations. In any case, as the light current increases in MoO_3/QDs/Si despite the presence of direct contact between MoO_3 and the Si_{H+}/Si layers that should contribute to its attenuation (as observed in samples containing no QD, Figure 7c,d), this highlights the occurrence of enhanced photocurrent generation in irradiated g-CS QDs. These results also indicate that proton-based treatments (and most likely other postgrowth processes that generate structural defects similar to those induced by proton bombardment) can be implemented to modify both the interface and the structure of core–shell QDs. Such processing could be done using plasma immersion ion implantation for ion doses between 10^{14} and 10^{18} ions cm^{-2} and ion energies between 20 eV and 10 keV, which is a low-cost technique suitable for high-throughput production in the solar

cell industry.[33] Hence, our study not only provides a better understanding of the proton irradiation effects on nanoscale devices but also promotes new technological routes based on wavefunction engineering to develop photovoltaic components with better light-to-current conversion efficiency, in particular, and tune the physical properties of QDs, in general.

3. Conclusion and Perspectives

In summary, we studied the effects of irradiation-induced damaging on both the structural and the optical properties of g-CS CdSe/CdS QDs using proton beams with acceleration voltages of 1.5 and 10.0 kV. SRIM Monte Carlo simulation code was applied to calculate the vacancies generated by impinging protons through g-CS QDs, demonstrating that the damage created by 1.5 keV protons in the CdS shell is 30% higher. TEM investigations conducted at high spatial resolution revealed the formation of nanocavities after high ion doses implantations. The PL and PL decay measurements conducted in all irradiated samples demonstrated that both PL intensity and lifetime of g-CS QDs decrease linearly with the concentration of structural defects generated in the CdS shell. *I–V* measurements carried out in dark and light environments show that the exposure to proton irradiations can significantly promote the photocurrent generation in g-CS QDs. This feature is associated with the delocalization of photoelectrons over the conduction bands of g-CS QDs, whose improvement with the formation of nonradiative structural defect is found to favor the electron–hole pair separation. In addition to providing physical insights in relation to charge carrier exchanges, bandgap alignment and exciton dissociation in systems containing g-CS QDs, such wavefunction engineering can be beneficial for potential applications in solar energy conversion and optical tuning, as well as for the development of new nanomaterials.

4. Experimental Section

Synthesis of g-CS QDs: CdSe QDs were first synthesized via a hot injection approach.[22,34] To grow the CdS shell layers on CdSe core (lattice mismatch: 3.9%) with retention of crystalline quality and minimal introduction of defects, the successive ionic layer adsorption and reaction (SILAR) approach[22,35] was implemented. This technique is based on the cation adsorption process and involves the presence of the van der Waals and electrostatic forces. The detailed procedure was described in Adhikari et al.[22] The QDs were then dispersed in toluene, to be spin-coated (1500 r min^{-1}, 60 s) as a thin g-CS QDs layer (≈20 nm) on fused silica substrates for irradiation experiments and optical measurements. According to the profilometry measurements (Bruker, Dektak XT) presented in the Supporting Information (Figure S8, Supporting Information), the g-CS QDs are not uniformly dispersed over the substrate. As the average diameter of g-CS QDs is lower than 10 nm and the spread g-CS QDs form an irregular layer of 20 nm average thickness, this means that some QDs are stacked on top of each other and form two monolayers of freestanding g-CS QDs.

Proton Radiation Experiments: The proton irradiation experiments were performed inside a low-energy ion accelerator, equipped with a magnet mass separator and a radio frequency plasma source. Ultrapure hydrogen gas was introduced into the source chamber, where positive ions were generated by stripping away electrons orbiting around the atomic nuclei. After extraction, these positive ions were accelerated and filtered using an electromagnet, to be then oriented toward the target sample. The total proton extraction/acceleration voltages were set at 1.5 and 10 kV for an implanted sample area of 0.81 cm^2 using a collimator. In this experiment, g-CS QDs were irradiated with fluences varying between 5×10^{13} and 1×10^{17} H^+ cm^{-2}, which are measured from a controlled proton beam current.

Characterizations: Freestanding g-CS QDs were dispersed on holey carbon film coated copper grid for TEM observation. BF images, SAED patterns, and HRTEM images were recorded using a JEOL JEM2100F TEM operating at 200 kV for all experiments. The PL spectroscopy measurements were conducted at room temperature using a 405 nm laser-diode excitation source (5.9 mW), as well as a QE65000 Ocean optics detector, for measurements in the visible (vis) range. The PL lifetime was measured using a time-correlated single-photon counting (TCSPC) mode with a 444 nm laser. TCSPC was based on the detection of single photons of a periodical light signal, the measurement of the detection times of the individual photons, and the reconstruction of the waveform from the individual time measurements. The measured decay curves were fitted using a triple exponential decay. The optical absorbance measurements were carried out between 200 and 700 nm at a scan speed of 600 nm min^{-1}, using a Cary 5000 UV–vis–NIR spectrophotometer (Varian).

I–V characterizations were conducted before and after proton irradiations, on pure Si substrates and g-CS QDs dispersed on Si p-type wafer, which were covered by a uniform MoO_3 layer of 20 nm thickness. Gold electrodes of 17 nm thickness were deposited by metal evaporation on the top of each studied sample, whose backside is bonded to a copper plate that is directly connected to the voltage source. The current through the device and the voltage across its two terminals were measured between −1.5 and + 1.5 V in dark environment and under light exposure, using a tungsten tip connected with the upper Au electrode and a compact solar simulator class AAA (Sciencetech SLB-300A) under 1 sun simulated sunlight (1 sun = AM 1.5G, 100 mW cm^{-2}), calibrated with a silicon reference cell. In order to check the reproducibility of the measurements, each *I–V* curve was recorded on 4–5 different Au electrodes that were designed on the same sample.

XPS and UPS investigations were conducted on MoO_3 films deposited on reference and implanted Si substrates using the monoenergetic Al Kα X-ray at 1486.6 eV and the He Iα emission at 21.22 eV, respectively.

Acknowledgements

F.R. acknowledges NSERC for funding through the individual Discovery Grants program and is grateful to the Canada Research Chairs program for funding and partial salary support. F.R. also acknowledges a Changjiang scholar award (Government of China) and Sichuan province for a 1000 talents short term award. G.S.S. acknowledges the UNESCO Chair in MATECSS for a PDF Excellence Scholarship and the funding from the University of Electronic Science and Technology of China and the China Postdoctoral Foundation (Grant No. Y02006023607941). H.G.Z. acknowledges the start funding support from Qingdao University and the funding from the Natural Science Foundation of Shandong Province (ZR2018MB001).

Conflict of Interest

The authors declare no conflict of interest.

Keywords

core–shell quantum dots, ion implantations, photocurrent generation, photoluminescence, transmission electron microcopy

[1] a) X.-M. Bai, A. F. Voter, R. G. Hoagland, M. Nastasi, B. P. Uberuaga, *Science* **2010**, *327*, 1631; b) M. Demkowicz, R. Hoagland, J. Hirth, *Phys. Rev. Lett.* **2008**, *100*, 136102; c) D. J. Bacon, Y. N. Osetsky, *Mater. Sci. Eng., A* **2004**, *365*, 46; d) X. Wei, D.-M. Tang, Q. Chen, Y. Bando, D. Golberg, *ACS Nano* **2013**, *7*, 3491; e) W. M. Parkin, A. Balan, L. Liang, P. M. Das, M. Lamparski, C. H. Naylor, J. A. Rodríguez-Manzo, A. C. Johnson, V. Meunier, M. Drndić, *ACS Nano* **2016**, *10*, 4134; f) T. Coenen, J. Van De Groep, A. Polman, *ACS Nano* **2013**, *7*, 1689; g) W. Jiang, J. A. Sundararajan, T. Varga, M. E. Bowden, Y. Qiang, J. S. McCloy, C. H. Henager Jr., R. O. Montgomery, *Adv. Funct. Mater.* **2014**, *24*, 6210.

[2] a) S. Bourdarie, M. Xapsos, *IEEE Trans. Nucl. Sci.* **2008**, *55*, 1810; b) M. Aguilar, D. Aisa, B. Alpat, A. Alvino, G. Ambrosi, K. Andeen, L. Arruda, N. Attig, P. Azzarello, A. Bachlechner, *Phys. Rev. Lett.* **2015**, *114*, 171103.

[3] a) R. Nasrin, M. Hasanuzzaman, N. Rahim, *Int. J. Energy Res.* **2018**, *42*, 1115; b) M. Yamaguchi, A. Khan, S. J. Taylor, M. Imaizumi, T. Hisamatsu, S. Matsuda, *IEEE Trans. Electron Devices* **1999**, *46*, 2133; c) J. H. Warner, R. J. Walters, S. R. Messenger, G. P. Summers, S. M. Khanna, D. Estan, L. S. Erhardt, A. Houdayer, *IEEE Trans. Nucl. Sci.* **2004**, *51*, 2887; d) D. Bätzner, A. Romeo, M. Terheggen, M. Döbeli, H. Zogg, A. Tiwari, *Thin Solid Films* **2004**, *451*, 536.

[4] a) T.-Y. Kim, K. Cho, W. Park, J. Park, Y. Song, S. Hong, W.-K. Hong, T. Lee, *ACS Nano* **2014**, *8*, 2774; b) W.-K. Hong, G. Jo, J. I. Sohn, W. Park, M. Choe, G. Wang, Y. H. Kahng, M. E. Welland, T. Lee, *ACS Nano* **2010**, *4*, 811.

[5] a) S. Muzafarova, S. Mirsagatov, F. Dzhamalov, *Semiconductors* **2009**, *43*, 175; b) A. A. Lebedev, A. M. Strel'chuk, V. V. Kozlovski, N. S. Savkina, D. V. Davydov, V. V. Solov'ev, *Mater. Sci. Eng., B* **1999**, *61*, 450.

[6] A. P. Alivisatos, *Science* **1996**, *271*, 933.

[7] a) C. D. Cress, S. M. Hubbard, B. J. Landi, R. P. Raffaelle, D. M. Wilt, *Appl. Phys. Lett.* **2007**, *91*, 183108; b) C.-H. M. Chuang, P. R. Brown, V. Bulović, M. G. Bawendi, *Nat. Mater.* **2014**, *13*, 796; c) X.-Y. Yu, J.-Y. Liao, K.-Q. Qiu, D.-B. Kuang, C.-Y. Su, *ACS Nano* **2011**, *5*, 9494; d) G. S. Selopal, H. Zhao, X. Tong, D. Benetti, F. Navarro-Pardo, Y. Zhou, D. Barba, F. Vidal, Z. M. Wang, F. Rosei, *Adv. Funct. Mater.* **2017**, *27*, 1701468; e) H. Zhao, F. Rosei, *Chem* **2017**, *3*, 229; f) L. Etgar, D. Yanover, R. K. Čapek, R. Vaxenburg, Z. Xue, B. Liu, M. K. Nazeeruddin, E. Lifshitz, M. Grätzel, *Adv. Funct. Mater.* **2013**, *23*, 2736.

[8] a) I. H. Campbell, B. K. Crone, *Adv. Mater.* **2006**, *18*, 77; b) S. Letant, T.-F. Wang, *Nano Lett.* **2006**, *6*, 2877; c) X. Gao, Q. Kang, J. Yeow, R. Barnett, *Nanotechnology* **2010**, *21*, 285502.

[9] a) Y. Zhou, H. Zhao, D. Ma, F. Rosei, *Chem. Soc. Rev.* **2018**, *47*, 5866; b) F. Navarro-Pardo, H. Zhao, Z. M. Wang, F. Rosei, *Acc. Chem. Res.* **2018**, *51*, 609; c) C. S. Erickson, L. R. Bradshaw, S. McDowall, J. D. Gilbertson, D. R. Gamelin, D. L. Patrick, *ACS Nano* **2014**, *8*, 3461.

[10] a) J. Caruge, J. E. Halpert, V. Wood, V. Bulović, M. Bawendi, *Nat. Photonics* **2008**, *2*, 247; b) B. N. Pal, Y. Ghosh, S. Brovelli, R. Laocharoensuk, V. I. Klimov, J. A. Hollingsworth, H. Htoon, *Nano Lett.* **2012**, *12*, 331; c) W. Deng, X. Xu, X. Zhang, Y. Zhang, X. Jin, L. Wang, S. T. Lee, J. Jie, *Adv. Funct. Mater.* **2016**, *26*, 4797.

[11] a) H. Zhu, N. Song, T. Lian, *J. Am. Chem. Soc.* **2011**, *133*, 8762; b) A. M. Smith, S. Nie, *Acc. Chem. Res.* **2010**, *43*, 190; c) S. S. Lo, T. Mirkovic, C. H. Chuang, C. Burda, G. D. Scholes, *Adv. Mater.* **2011**, *23*, 180.

[12] N. N. Hewa-Kasakarage, P. Z. El-Khoury, A. N. Tarnovsky, M. Kirsanova, I. Nemitz, A. Nemchinov, M. Zamkov, *ACS Nano* **2010**, *4*, 1837.

[13] a) D. Dorfs, T. Franzl, R. Osovsky, M. Brumer, E. Lifshitz, T. A. Klar, A. Eychmüller, *Small* **2008**, *4*, 1148; b) M. Jones, S. Kumar, S. S. Lo, G. D. Scholes, *J. Phys. Chem. C* **2008**, *112*, 5423.

[14] a) G. Rizza, P. Coulon, V. Khomenkov, C. Dufour, I. Monnet, M. Toulemonde, S. Perruchas, T. Gacoin, D. Mailly, X. Lafosse, *Phys. Rev. B* **2012**, *86*, 035450; b) D. Bufford, S. H. Pratt, T. J. Boyle, K. Hattar, *Chem. Commun.* **2014**, *50*, 7593.

[15] T. Järvi, D. Pohl, K. Albe, B. Rellinghaus, L. Schultz, J. Fassbender, A. Kuronen, K. Nordlund, *EPL* **2009**, *85*, 26001.

[16] D. Pacifici, E. Moreira, G. Franzo, V. Martorino, F. Priolo, F. Iacona, *Phys. Rev. B* **2002**, *65*, 144109.

[17] a) R. Leon, G. Swift, B. Magness, W. Taylor, Y. Tang, K. Wang, P. Dowd, Y. Zhang, *Appl. Phys. Lett.* **2000**, *76*, 2074; b) R. Leon, S. Marcinkecius, J. Siegert, B. Cechavicius, B. Magness, W. Taylor, C. Lobo, *IEEE Trans. Nucl. Sci.* **2002**, *49*, 2844.

[18] a) W. Lu, Y. Ji, G. Chen, N. Tang, X. Chen, S. Shen, Q. Zhao, M. Willander, *Appl. Phys. Lett.* **2003**, *83*, 4300; b) Y. Ji, G. Chen, N. Tang, Q. Wang, X. Wang, J. Shao, X. Chen, W. Lu, *Appl. Phys. Lett.* **2003**, *82*, 2802.

[19] E. Zanazzi, M. Favaro, A. Ficorella, L. Pancheri, G. Dalla Betta, A. Quaranta, *Opt. Mater.* **2019**, *88*, 271.

[20] J. F. Ziegler, M. D. Ziegler, J. P. Biersack, *Nucl. Instrum. Methods Phys. Res., Sect. B* **2010**, *268*, 1818.

[21] R. E. Algra, M. A. Verheijen, M. T. Borgström, L.-F. Feiner, G. Immink, W. J. van Enckevort, E. Vlieg, E. P. Bakkers, *Nature* **2008**, *456*, 369.

[22] R. Adhikari, L. Jin, F. Navarro-Pardo, D. Benetti, B. AlOtaibi, S. Vanka, H. Zhao, Z. Mi, A. Vomiero, F. Rosei, *Nano Energy* **2016**, *27*, 265.

[23] D. B. Williams, *Transmission Electron Microscopy*, Springer Science & Business Media, New York **2009**.

[24] H. Zhao, Z. Fan, H. Liang, G. Selopal, B. Gonfa, L. Jin, A. Soudi, D. Cui, F. Enrichi, M. Natile, *Nanoscale* **2014**, *6*, 7004.

[25] H. Zhao, D. Benetti, L. Jin, Y. Zhou, F. Rosei, A. Vomiero, *Small* **2016**, *12*, 5354.

[26] G. Schlegel, J. Bohnenberger, I. Potapova, A. Mews, *Phys. Rev. Lett.* **2002**, *88*, 137401.

[27] A. Van Dijken, E. A. Meulenkamp, D. Vanmaekelbergh, A. Meijerink, *J. Phys. Chem. B* **2000**, *104*, 1715.

[28] A. Borgschulte, O. Sambalova, R. Delmelle, S. Jenatsch, R. Hany, F. Nüesch, *Sci. Rep.* **2017**, *7*, 40761.

[29] a) J. Meyer, S. Hamwi, M. Kröger, W. Kowalsky, T. Riedl, A. Kahn, *Adv. Mater.* **2012**, *24*, 5408; b) Y. Wu, H. Wang, W. Tu, S. Wu, J. W. Chew, *Appl. Organomet. Chem.* **2019**, *33*, e4780.

[30] S. Shen, J. Chen, M. Wang, X. Sheng, X. Chen, X. Feng, S. S. Mao, *Prog. Mater. Sci.* **2018**.

[31] D. Nesheva, *Solid-State Electron.* **1987**, *30*, 173.

[32] B. Blackman, D. M. Battaglia, T. D. Mishima, M. B. Johnson, X. Peng, *Chem. Mater.* **2007**, *19*, 3815.

[33] D. L. Young, W. Nemeth, V. LaSalvia, M. R. Page, S. Theingi, J. Aguiar, B. G. Lee, P. Stradins, *Sol. Energy Mater. Sol. Cells* **2016**, *158*, 68.

[34] B. O. Dabbousi, J. Rodriguez-Viejo, F. V. Mikulec, J. R. Heine, H. Mattoussi, R. Ober, K. F. Jensen, M. G. Bawendi, *J. Phys. Chem. B* **1997**, *101*, 9463.

[35] Y. Ghosh, B. D. Mangum, J. L. Casson, D. J. Williams, H. Htoon, J. A. Hollingsworth, *J. Am. Chem. Soc.* **2012**, *134*, 9634.